

# Algorithmic Improvements to a High-Order Space Marching Method for Sonic Boom Propagation

Jeffrey Housman <sup>\*</sup>, James Jensen <sup>†</sup>, Gaetan Kenway <sup>‡</sup> and Cetin Kiris <sup>§</sup>

*NASA Ames Research Center, M/S/ 258-2, Moffett Field, CA 94035*

**Abstract:** Algorithmic improvements to a high-order space marching method enabling an efficient strategy for sonic boom propagation by coupling near-field Computational Fluid Dynamics (CFD) solutions to an efficient space marching solver are described. The space marching solver is based on a high-order accurate finite-difference discretization of the 3D Euler equations on a specially designed curvilinear grid to enable a single sweep space marching solution. The improvements to the existing space marching method [1] include enhancements to the automatically generated grid, elliptic hole cutting, and generalization of the coupling to both structured and unstructured grid CFD solvers. The coupled approach is shown to improve efficiency and accuracy by reducing the necessary domain size of the CFD grid and generating mid-field solutions from coarse CFD grids equivalent to those obtained using fine grid CFD. This is demonstrated using test cases from the AIAA Sonic Boom Prediction Workshops and four different CFD solvers.

*Keywords:* Numerical Algorithms, Aeroacoustics, Sonic Boom.

## 1 Introduction

The National Aeronautics and Space Administration (NASA) in collaboration with industry partners is currently developing the X-59, a supersonic aircraft which is shaped to reduce the loudness of the sonic boom. It was established in Housman *et. al.* [1] that a three-step procedure consisting of near-field CFD, high-order space marching, and far-field acoustic propagation resulted in an efficient and accurate method for ground level noise predictions using approximately half the computational resources as the conventional two-step procedure. Moreover, the efficiency gain of utilizing the space marching method facilitated the study of extending the radial coupling location with the far-field acoustic propagation code. It was demonstrated that a minimum of four body lengths was necessary to include all relevant three-dimensional azimuthal velocity effects on the ground level noise prediction. In addition, Duensing *et. al.* [2] showed that the radial extent of the CFD domain size could be significantly reduced to approximately half a body length with no loss of accuracy in ground level noise prediction when coupled to the high-order space marching solver.

Two distinct approaches have been reported in the literature for propagating the nonlinear pressure waves from the near-field to a distance appropriate for far-field acoustic propagation. The first approach utilizes a multi-pole matching procedure [3, 4, 5, 6] based on the expansion derived by George [7]. This method relies on projecting the near-field CFD solution onto a sequence of multi-pole distributions representing the Whitham F-function [8]. Then at each azimuth, the far-field F-function representation is used as input into the far-field propagation code. The success of this approach not only relies on the accuracy of the multi-pole expansion, but also on the procedure which projects the near-field CFD solution onto the multi-pole basis. The second method utilizes the Euler equations (or reduced forms) directly, including the full-potential equation [9, 10], or a space marching approach [11, 12, 13]. It is the space marching method that is used in the present work.

---

<sup>\*</sup>Research Scientist, Computational Aerosciences Branch

<sup>†</sup>Research Scientist, Computational Aerosciences Branch

<sup>‡</sup>Research Scientist, Science and Technology Corporation

<sup>§</sup>Branch Chief, Computational Aerosciences Branch

Space marching is a numerical technique applied to the Euler or Parabolized Navier-Stokes equations developed in the 1970's [14, 15, 16] as an efficient solution procedure for three-dimensional supersonic flows. By marching, either explicitly or implicitly, in the streamwise direction, the three-dimensional problem is reduced to an unsteady-like two-dimensional one with significant savings in both storage and runtime. In the 1980's, the method was extended to flows with subsonic pockets [17], equilibrium air computations around hypersonic vehicles [18], and upwind total variation diminishing (TVD) algorithms [19]. As high-performance computing resources became more widely available and distributed memory machines became affordable, time-marching methods became more attractive since a dominant flow direction is not necessary for steady-state convergence. Nevertheless, some groups have continued to mature space marching methods [20, 21, 22, 23] because of their fast convergence properties and computational efficiency for predominantly supersonic flow-fields.

In this work, algorithmic improvements to the high-order space marching method, described in Housman *et. al.* [1], to enable accurate and efficient sonic boom propagation by coupling to either structured or unstructured CFD near-field solutions are described. First, the computational methodology is provided including the governing equations, automated Mach-cone aligned space marching grid generation and high-order numerical discretization along with implicit solution procedure. The automatically generated grid is enhanced to retain a valid space marching mesh as the local Mach number approaches unity and an elliptic hole cutting procedure is introduced that allows coupling with the CFD solution closer to the aircraft, further reducing the accuracy requirements of the CFD. Next, a series of results are presented demonstrating the use of the space marching solver coupled with different near-field CFD solutions. A generalization of the coupling code allowing the space marching solver to couple with either structured or unstructured grid CFD solutions will be demonstrated using test cases from the AIAA Sonic Boom Prediction Workshops. Unstructured grid solutions provided to the workshop by USM3D and HALO3D, along with structured overset grid solutions provided by LAVA are utilized. Finally, a local error analysis procedure following Anderson *et. al.* [24] is used to assess uncertainty in the space marching grid resolution for a select case from the workshop.

## 2 Computational Methodology

Nonlinear wave propagation from low-boom supersonic aircraft requires accurate and efficient numerical methods which fit well within the context of space marching methods. The high-order accurate space marching algorithm described in this work was developed within the Launch, Ascent, and Vehicle Aerodynamics (LAVA) framework. The space marching method utilizes similar high-order finite-difference methods and overset grid interpolation routines as those used in the curvilinear CFD solver in LAVA [25]. A diagram of the three-step procedure [1]: 1.) surface to near-field CFD, 2.) near-field to mid-field space marching, 3.) mid-field to ground far-field acoustic propagation is shown in Figure 1(a) along with an example of the space marching solution illustrating the elliptical hole interface with the CFD near-field in Figure 1(b).

To begin, the governing equations in a general curvilinear coordinate system are presented. Next, the automated Mach-cone aligned curvilinear grid generation method is described along with elliptic hole cutting procedure. Last, the numerical discretization and implicit space marching solution approach is outlined.

### 2.1 Governing Equations

The equations governing the evolution of the near-field supersonic flow to the mid-field are the steady-state Euler equations of gas dynamics. Definition of the space marching flow domain, near-field to mid-field, starts with an elliptical region around the aircraft with major axis of approximately 0.5 to 1.5 span and minor axis chosen close to the fuselage extent. The ellipse extends to a radial distance of approximately 10 body lengths from the aircraft. This can be extended as far as local atmospheric effects, such as hydrostatic balance and thermal stratification, are negligible. The steady Euler equations are written for a general curvilinear coordinate system in strong conservation law form [26] as,

$$\frac{\partial \hat{E}}{\partial \xi} + \frac{\partial \hat{F}}{\partial \eta} + \frac{\partial \hat{G}}{\partial \zeta} = 0, \quad (1)$$

where

$$\hat{E} = \begin{bmatrix} \rho\hat{U} \\ \rho\hat{U}u + p\hat{\xi}_x \\ \rho\hat{U}v + p\hat{\xi}_y \\ \rho\hat{U}w + p\hat{\xi}_z \\ \rho\hat{U}H \end{bmatrix}, \quad \hat{F} = \begin{bmatrix} \rho\hat{V} \\ \rho\hat{V}u + p\hat{\eta}_x \\ \rho\hat{V}v + p\hat{\eta}_y \\ \rho\hat{V}w + p\hat{\eta}_z \\ \rho\hat{V}H \end{bmatrix}, \quad \hat{G} = \begin{bmatrix} \rho\hat{W} \\ \rho\hat{W}u + p\hat{\zeta}_x \\ \rho\hat{W}v + p\hat{\zeta}_y \\ \rho\hat{W}w + p\hat{\zeta}_z \\ \rho\hat{W}H \end{bmatrix}. \quad (2)$$

Standard notation is used where  $\rho$  is the density,  $p$  the pressure,  $(u, v, w)$  the Cartesian velocity components, and  $H = h + \frac{1}{2}(u^2 + v^2 + w^2)$  is the total enthalpy. The contravariant velocities in the  $(\xi, \eta, \zeta)$  coordinate directions are denoted

$$\hat{U} = u\hat{\xi}_x + v\hat{\xi}_y + w\hat{\xi}_z, \quad \hat{V} = u\hat{\eta}_x + v\hat{\eta}_y + w\hat{\eta}_z, \quad \hat{W} = u\hat{\zeta}_x + v\hat{\zeta}_y + w\hat{\zeta}_z. \quad (3)$$

Note the metric relations have been scaled by the Jacobian of the metric transformation

$$\left(\hat{\xi}_x, \hat{\xi}_y, \hat{\xi}_z\right) = J^{-1}(\xi_x, \xi_y, \xi_z), \quad \left(\hat{\eta}_x, \hat{\eta}_y, \hat{\eta}_z\right) = J^{-1}(\eta_x, \eta_y, \eta_z), \quad \left(\hat{\zeta}_x, \hat{\zeta}_y, \hat{\zeta}_z\right) = J^{-1}(\zeta_x, \zeta_y, \zeta_z). \quad (4)$$

The equation set is closed by the ideal gas law which relates  $p = \rho RT$ , where  $R = C_p(\gamma - 1)/\gamma$ ,  $C_p$  is the specific heat at constant pressure, and  $\gamma$  is the ratio of specific heats.

## 2.2 Mach-cone Aligned Space Marching Grid

A specially designed structured curvilinear grid is used to discretize the space between the near-field and mid-field. Structured curvilinear grids have several advantages over unstructured, structured cylindrical, and Cartesian grids for this particular application. The advantages over unstructured grids include the high efficiency and low memory footprint of the corresponding numerical algorithm and the straightforward and relatively inexpensive extension to high-order low-dissipation finite-difference discretizations which are extremely efficient for weakly nonlinear wave propagation. The main advantage over structured cylindrical and Cartesian grids are the ability to create a Mach-cone aligned mesh for each azimuth within a single grid. The advantage of using Mach-cone aligned grids for nonlinear wave propagation in low boom environments has been shown by several groups [27, 28]. One of the first publications demonstrating the use of Mach-cone aligned grids was Siclari and Darden [12], where they used a cylindrical/spherical coordinate system with Mach-cone alignment for the bow shock to capture sonic booms from simplified fuselage wing configurations and propagate them to the mid-field. In fact, the advantage of Mach-cone alignment is so advantageous, that when using adjoint based mesh adapted Cartesian grids, it was found to be more efficient to solve for a single azimuth of interest (or a tight range) independently, while insuring Mach-cone alignment with respect to that azimuth, than to try and solve for all azimuths at once [24].

Inspired by the grid topology used in Siclari and Darden [12] and implicit solution strategies used in overset grid methods, a specially designed structured curvilinear, Mach-cone aligned, cylindrical-like automated grid generation procedure, which utilizes *ibanking* overset grid technology, was established in Housman *et. al.* [1]. It was determined that orthogonality on the  $(\xi, \zeta)$  plane requires a local Mach in the free-stream direction greater than 1.42. Since many of the low-boom supersonic aircraft designs are targeting cruise Mach numbers ranging from 1.2 - 1.4, a modification to the original space marching grid generator was necessary to maintain a valid space marching direction. Figures 2(a) - (c) show a side view, front view, and an isometric view of a coarse space marching grid. The key to maintaining a valid space marching direction is to align the  $\zeta$ -coordinate direction with the freestream flow direction. Provided the local Mach number in the freestream direction remains above unity, the space marching solution algorithm remains valid. This will be guaranteed provided the elliptic hole interface between the CFD near-field grid and the space marching grid is located outside the very thin boundary layer of the aircraft (and the freestream Mach is above one of course). Once the  $\zeta$ -coordinate direction is defined the  $\xi$ -coordinate direction is constructed to maintain Mach-cone alignment. As mentioned previously, this reduces the effective amount of artificial dissipation, since closely aligning a coordinate direction with the characteristic surfaces of the solution results in less error. This is simply because the solution is constant along the characteristic surfaces and even a first-order accurate numerical scheme can capture a constant solution exactly. Finally, the  $\eta$ -coordinate is chosen to be the

circumferential direction which is a simple and efficient way to cover the three-dimensional domain that remains consistent with the characteristic surfaces of the solution. Note, the observant reader may realize the mesh will have regions of negative volume cells near the axis, this is handled using a *blanking* procedure described next.

In addition to the re-orientation of the space marching direction to maintain a valid marching direction if the local Mach number approaches unity, another major improvement in the automated grid generation procedure is in the hole cutting definition. In the original approach [1], a cylindrical hole cutting definition was used to *blank*, or mark, selected grid points from the space marching grid to effectively remove them from the grid system. The blanked region of the space marching domain requires the near-field CFD solution to be used within this region, and this solution must be accurate. This implies that reducing the blanked region will reduce the accuracy requirements of the near-field CFD, which effectively means that the CFD grid can be coarsened faster outside of the blanked region. In the new modified approach this is accomplished by generalizing the cylindrical hole cut with an elliptical hole cut defined using the following equation,

$$\sqrt{a_0 (y - y_0)^2 + b_0 (z - z_0)^2} = 1. \quad (5)$$

The coordinates  $y_0$  and  $z_0$  define the center of the ellipse while the coefficients  $a_0$  and  $b_0$  control the major and minor axis of the ellipse. Note the ellipsoidal hole cut is performed before the space marching grid is rotated into the freestream flow direction and choosing the free-parameters is currently performed by the user. Automation of this process is currently being explored along with more elaborate implicit hole cutting strategies. The current elliptical hole cutting process was deemed efficient and easy for users to understand. Figures 3(a) - (b) plot a comparison between the original cylindrical hole cutting definition (shown in blue) and the new elliptical hole cutting definition (shown in red). It is evident that the space marching domain, which starts outside of the hole cutting surface, begins much closer to the aircraft using an ellipsoid versus a cylinder, especially the region directly below the vehicle which is the predominate contributor for ground level noise. Presuming the space marching method is more accurate than traditional CFD methods, which will be demonstrated in this work, implies the closer interface location obtained by the elliptical hole cut is superior.

### 2.3 Numerical Discretization

Now that the structured grid and associated curvilinear coordinate directions are established, the numerical discretization procedure is described. The space marching direction is defined to be in the  $\zeta$ -coordinate direction. The choice of using the  $\zeta$ -coordinate as the space marching direction allows for a cache-friendly implementation on modern computer hardware. The  $\eta$  coordinate is assigned to the circumferential direction, and  $\xi$  is used for the remaining coordinate direction. Two distinct approaches to the derivative approximations are used to discretize the governing equations depending on the coordinate direction. In the space marching direction, backward differencing formulas are utilized to discretize the flux derivative. These are typically used for discretizing the time-derivative in unsteady Navier-Stokes calculations, and are a natural choice for the space marching direction since the waves can only travel in the positive  $\zeta$ -coordinate direction on the specially designed grid. Three different orders of accuracy for backward differencing are implemented in the current space marching solver; first-order, second-order, and third-order

$$\frac{\partial \hat{G}}{\partial \zeta} \approx \frac{\hat{G}_l - \hat{G}_{l-1}}{\Delta \zeta} \quad (\text{first-order}), \quad (6)$$

$$\frac{\partial \hat{G}}{\partial \zeta} \approx \frac{3(\hat{G}_l - \hat{G}_{l-1}) - (\hat{G}_{l-1} - \hat{G}_{l-2})}{2\Delta \zeta} \quad (\text{second-order}), \quad (7)$$

$$\frac{\partial \hat{G}}{\partial \zeta} \approx \frac{11(\hat{G}_l - \hat{G}_{l-1})}{6\Delta \zeta} - \frac{7(\hat{G}_{l-1} - \hat{G}_{l-2})}{6\Delta \zeta} + \frac{(\hat{G}_{l-2} - \hat{G}_{l-3})}{3\Delta \zeta} \quad (\text{third-order}). \quad (8)$$

In the cross-stream directions, a high-order Hybrid Weighted Compact Nonlinear Scheme (HWCNS) [29, 30, 31] is used to approximate the  $(\xi, \eta)$  derivatives. The HWCNS utilizes a central difference stencil that combines numerical fluxes at the edges with physical fluxes at the nodes resulting in high spectral accuracy,

which is important for weakly nonlinear wave propagation. An example of the HWCNS discretization applied to the  $\xi$ -coordinate convective flux is,

$$\frac{\partial \hat{E}}{\partial \xi} \approx \frac{a_1 \left( \tilde{E}_{j+1/2} - \tilde{E}_{j-1/2} \right) + a_2 \left( \hat{E}_{j+1} - \hat{E}_{j-1} \right)}{\Delta \xi}. \quad (9)$$

The coefficients  $a_1$  and  $a_2$  can be chosen to obtain either second (HWCNS2) or fourth (HWCNS4) order accuracy. The step-sizes  $\Delta \xi$  and  $\Delta \zeta$  have been taken to be unity. A similar formula is available for the  $\eta$ -coordinate derivative. The artificial dissipation in the scheme is introduced through the numerical fluxes at the edges,  $\tilde{E}_{j+1/2}(Q_L, Q_R)$ , which are constructed with a modified Roe numerical flux [32, 33, 34] with left and right state interpolations,  $Q_L$  and  $Q_R$ , generated from a high-order WENO interpolation [35]. In the current implementation, third and fifth order accurate upwind biased WENO interpolations (WENO3 and WENO5) and an improved fifth-order accurate WENO interpolation [36] (ZWENO5) is available.

It is well known that free-stream preservation (i.e. the GCL condition) requires that identical finite-difference operators are used to compute the metric terms, as those used to discretize the convective flux derivatives [37, 38, 39]. The derivatives which appear in the metric term evaluations for the  $(\xi, \eta)$ -coordinate directions utilize the same HWCNS as that used for the convective flux where the required *half-point* grid values are obtained from central interpolations of the same order as the derivative evaluation. In the space marching direction, the metric terms are evaluated with the BDF formulas above. Evaluating the metric terms using standard central differencing, or using the HWCNS in the space marching direction leads to a breakdown in free-stream preservation. Examples of this were shown in Housman *et. al.* [1].

To summarize, the nonlinear discrete residual operator at an arbitrary space marching  $\zeta$  surface plane  $l$ , and  $(\xi, \eta)$  grid point location  $(j, k)$ , is written as,

$$\begin{aligned} R_{j,k,l} &= a_1 \left( \tilde{E}_{j+1/2} - \tilde{E}_{j-1/2} \right) + a_2 \left( \hat{E}_{j+1} - \hat{E}_{j-1} \right) \\ &+ a_1 \left( \tilde{F}_{k+1/2} - \tilde{F}_{k-1/2} \right) + a_2 \left( \hat{F}_{k+1} - \hat{F}_{k-1} \right) \\ &+ \left( \delta_{\zeta}^{(BDF)} \hat{G} \right)_l \end{aligned} \quad (10)$$

(11)

This represents a system of nonlinear equations, on the surface of constant  $l$ , which must be iteratively solved. Once the system is solved on this surface, the solution on the next surface,  $l + 1$ , can be found. An efficient implicit solution procedure is described next.

## 2.4 Implicit Space Marching Solution Procedure

In the single sweep space marching procedure, the solution is marched in the  $\zeta$ -coordinate direction starting from an interpolated CFD solution on the inner ellipsoid of fringe points,  $Q_{fringe} = \text{Interp}(Q_{\text{CFD}})$ . At each new streamwise station, the nonlinear system of equations is solved on the  $(\xi, \eta)$  plane with the evaluation of  $\hat{G}_{l-1}$  and  $\hat{G}_{l-2}$  (and perhaps  $\hat{G}_{l-3}$ ) set from the previous  $(\xi, \eta)$  plane solutions. Only a single sweep is necessary provided the contravariant Mach number in the streamwise direction is greater than one,  $\hat{M}_{\zeta} = \hat{W}/\hat{c} > 1$ , for all streamwise stations. This condition is satisfied when using the specially designed structured curvilinear grid and results in a reduced nonlinear system of equations where only the solution of the current plane  $Q_l$  is unknown for all  $(j, k)$ . Introducing the iteration parameter,  $m$ , and assuming a first-order discretization in the cross-marching directions, the system at the next  $l + 1$  plane can be represented as,

$$\begin{aligned} \mathcal{R}(Q_{m+1}, Q_l, Q_{l-1}) &= \left( \tilde{E}_{j+1/2, m+1} - \tilde{E}_{j-1/2, m+1} \right) + \left( \tilde{F}_{j+1/2, m+1} - \tilde{F}_{j-1/2, m+1} \right) \\ &+ \frac{3}{2} \left( \hat{G}_{m+1} - \hat{G}_l \right) - \frac{1}{2} \left( \hat{G}_l - \hat{G}_{l-1} \right). \end{aligned} \quad (12)$$

Now each term depending on  $m + 1$  can be linearized about the previous iteration (on the current  $l + 1$  plane),

$$\begin{aligned}\tilde{E}_{j+1/2,m+1} &\approx \tilde{E}_{j+1/2,m} + \left(\frac{\partial \tilde{E}_{j+1/2,m}}{\partial Q_{j+1,m}}\right) \Delta Q_{j+1,m} + \left(\frac{\partial \tilde{E}_{j+1/2,m}}{\partial Q_{j,m}}\right) \Delta Q_{j,m} \\ \tilde{F}_{k+1/2,m+1} &\approx \tilde{F}_{k+1/2,m} + \left(\frac{\partial \tilde{F}_{k+1/2,m}}{\partial Q_{k+1,m}}\right) \Delta Q_{k+1,m} + \left(\frac{\partial \tilde{F}_{k+1/2,m}}{\partial Q_{k,m}}\right) \Delta Q_{k,m} \\ \hat{G}_{m+1} &\approx \hat{G}_m + \left(\frac{\partial \hat{G}_m}{\partial Q_m}\right) \Delta Q_m.\end{aligned}$$

Using the above linearization and introducing a pseudo-time stepping term to improve convergence during the early stages of the nonlinear planar relaxation procedure, Equation 12 can be rewritten as,

$$\begin{aligned}& - \left(\frac{\partial \tilde{F}_{k-1/2,m}}{\partial Q_{k-1,m}}\right) \Delta Q_{k-1,m} - \left(\frac{\partial \tilde{E}_{j-1/2,m}}{\partial Q_{j-1,m}}\right) \Delta Q_{j-1,m} \\ & + \left[ \frac{3}{2} \frac{\Gamma}{J \Delta \tau} + \left(\frac{\partial \tilde{E}_{j+1/2,m}}{\partial Q_{j,m}}\right) - \left(\frac{\partial \tilde{E}_{j-1/2,m}}{\partial Q_{j,m}}\right) + \left(\frac{\partial \tilde{F}_{k+1/2,m}}{\partial Q_{k,m}}\right) - \left(\frac{\partial \tilde{F}_{k-1/2,m}}{\partial Q_{k,m}}\right) \right] \Delta Q_{j,k,m} \quad (13) \\ & + \left(\frac{\partial \tilde{E}_{j+1/2,m}}{\partial Q_{j+1,m}}\right) \Delta Q_{j+1,m} + \left(\frac{\partial \tilde{F}_{k+1/2,m}}{\partial Q_{k+1,m}}\right) \Delta Q_{k+1,m} \\ & = -\mathcal{R}(Q_m, Q_l, Q_{l-1}),\end{aligned}$$

where  $\Gamma = \partial W / \partial Q$  is the change of variables matrix from conservative variables  $W$  to primitive variables  $Q$ . Utilizing a defect-correction approach the first-order right-hand-side,  $\mathcal{R}$ , is replaced with the high-order accurate discretization,  $R$  in Equation 10. *Blanked* points are handled by replacing the left-hand-side blocks by the identity matrix on the diagonal and setting the right-hand-side to zero. The *fringe* points, which are the points where the solution is interpolated from the near-field CFD solution, are also handled similarly with left-hand-side blocks replaced by the identity matrix and right-hand side zero, but the solution values  $Q$  are set to the interpolated valued during initialization. This decouples both the *blanked* and *fringe* points from the system of equations. Equation 13 is approximately solved to obtain a quasi-Newton correction  $\Delta Q_m$ . As the iteration procedure converges  $m \rightarrow \infty$ , the norm of the high-order residual converges and the nonlinear system of equations at that plane is satisfied ( $\|R\| \rightarrow 0$  and  $Q_m \rightarrow Q_{l+1}$ ). In the current implementation an alternating line-implicit Jacobi relaxation procedure in the  $(\xi, \eta)$ -coordinate directions is used.

### 3 Results

The high-order single sweep space marching method described above is used to propagate several near-field CFD solutions for different low-boom aircraft geometries from the Second and Third AIAA Sonic Boom Prediction Workshops. First a demonstration of CFD domain reduction is provided using structured overset grid solutions for the C608 test case from the Third AIAA Sonic Boom Prediction Workshop provided by Duensing *et. al.* [2]. Second, the generalization of the CFD coupling from structured overset grid CFD solutions to unstructured grid solutions is demonstrated using USM3D solutions on the C608 aircraft provided by Elmiligui *et. al.* [40]. Next, the accuracy enhancement capability of the space marching method is demonstrated using the sequence of coarse, medium, and fine grid CFD results for the C608 provided to the workshop by Ozcer *et. al.* [41] of ANSYS Canada. Finally, an automated local error analysis method based on Richardson extrapolation is described and used to evaluate the space marching grid resolution sensitivity on the JAXA Wing Body (JWB) from the Second AIAA Sonic Boom Prediction Workshop.

### 3.1 CFD Domain Reduction

Results from the CFD domain reduction for the C608 were originally published in Duensing *et. al.* [2] and repeated here for completeness of this work. A domain of dependence study is performed to determine the required radial extent of the CFD domain. This analysis consisted of constructing a forward opening Mach cone placed just upstream of the nose of the vehicle and a Mach cone opening in the opposite direction placed near the aft of the vehicle. The placement of these cones along the streamwise axis was adjusted until the entire vehicle geometry was encompassed by the two cones. The radius where the cones intersect,  $R/L_{body} = 0.53$ , provides a good estimate of the required radial domain extent. Figure 4 (a) shows the intersection of the two Mach cones along with the C608 vehicle located within the two cones.

#### 3.1.1 Domain of Dependence Results

Using the Mach-cone based domain of dependence a modified off-body CFD grid script was generated which allows the user to input the desired radial extent of the off-body grid. Figure 4 (b) shows the resulting off-body grids for the three radial CFD domain extents of interest;  $R/L_{body} = 0.53$  the minimum required radial extent contains a total of 149 million grid points including the medium resolution near-body grids;  $R/L_{body} = 4$  based on the workshop specification of the sBOOM coupling at  $R/L_{body} = 3$  which is 178 million grid points; and  $R/L_{body} = 7$  for sensitivity analysis of sBOOM coupling location at  $R/L_{body} = 6$  which contains 203 million grid points. The  $R/L_{body} = 0.53$  grid results in a 16 percent reduction in grid points compared to the  $R/L_{body} = 4$  grid, and a 26.5 percent reduction compared to the  $R/L_{body} = 7$  grid.

CFD solutions for the three grids were generated using the LAVA structured curvilinear overset grid solver. A comparison of the pressure field on a cylinder at  $R/L_{body} = 0.25$  is plotted for domain extents of  $R/L_{body} = 4$  and  $R/L_{body} = 0.53$  in Figs. 5 (a) and (b) respectively. This location is near the coupling location of the space marching grid which will be described in more detail in the next section. There is no visible difference between the two solutions at the pressure scales included in the plots. This implies that the simplified domain of dependence study is sufficient for the C608 vehicle. Examining the on-track pressure signature at  $R/L_{body} = 0.25$  in Figure 6, no difference in the pressure signatures is observed. In the next two sections the reduced CFD domain will be used as input into the space marching solver and the resulting pressure field will be compared with the larger CFD domain results.

#### 3.1.2 Space Marching Grid and Solution

Figure 7 (a) - (d) shows several views of a coarse grid version of the space marching grid. The radial domain extent was set to  $R/L_{body} = 10$  to enable sBOOM coupling up to  $R/L_{body} = 9$ . The space marching direction is oriented in the streamwise direction and the solution starts at the first upstream plane and marches downstream. The first three layers of nodes outside of the user-defined elliptic hole cutting surface, denoted "fringe" points, are used to couple the CFD solution to the space marching grid. The fringe points are illustrated in the Figure 7 (d), the CFD solution is interpolated at these locations and used as boundary conditions during the space marching solution procedure. Three space marching grid resolutions were generated with  $\Delta s/L_{body} = 0.006$ , 0.003, and 0.0015 which resulted in 18.9 million, 72.3 million, and 285.4 million grid points respectively.

The fourth-order Hybrid Weighted Compact Nonlinear scheme with third-order WENO interpolation is used in the non-space marching direction, while the second order backward differencing scheme is used in the space marching direction. The two-dimensional non-linear system is solved at each space marching station using an alternating line Jacobi relaxation procedure, and the  $L2$ -norm of the residual is reduced by two orders of magnitude before marching to the next station. For the three space marching grids used in this study, the space marching solution time required 44 seconds, 139 seconds, and 440 seconds respectively, using 80 OpenMP threads on a modern high-end workstation. These computational resources are negligible compared to the cost of the CFD ( $\mathcal{O}(100 - 1000)$  CPU core hours) even on the finest space marching grid.

In order to establish the necessary mesh resolution for the space marching grid, the near-field pressure signatures are compared to the CFD solution. Figures 8 (a) - (d) plot the pressure signatures at  $R/L_{body} = 3$  and 6 both on-track ( $\phi = 0^\circ$ ) and off-track ( $\phi = 30^\circ$ ) for the CFD as well as for the three space marching grid resolutions considered. Noticeable differences between the CFD and the coarsest space marching grid resolution,  $\Delta s/L_{body} = 0.006$ , are observed. The medium and fine space marching grid resolutions,

$\Delta s/L_{body} = 0.003$  and  $0.0015$  are essentially on-top of the CFD. An inset image of the wave-train created by the wing are included in each image. Examination of the inset images shows a minor discrepancy between the medium space marching grid resolution and the CFD. The fine space marching grid solution is indistinguishable from the CFD. From this analysis, the  $\Delta s/L_{body} = 0.0015$  space marching grid resolution is chosen for far-field propagation with sBOOM.

Three radial coupling locations were analyzed for coupling the space marching solution with sBOOM,  $R/L_{body} = 3, 6,$  and  $9$ . The closer two locations were also propagated using the  $R/L_{body} = 7$  CFD solution. Figure 9 (a) plots a comparison of the ground signatures using the space marching and CFD solutions coupled at  $R/L_{body} = 3$ . The two ground signatures are almost identical with only a minor discrepancy between  $120 - 130$  ms. The difference in the perceived loudness (PL) level is  $0.2$  dB between the solutions with the space marching solution producing a PL of  $77.9$  dB and the CFD generating  $77.7$  dB. A similar comparison is shown in Figure 9 (b) but with coupling location extended to  $R/L_{body} = 6$ . Again, there is almost no difference in the ground signatures with the same minor discrepancy between  $120 - 130$  ms. As in the previous analysis, a  $0.2$  dB difference is observed in the PL but the levels are slightly elevated to a PL of  $78$  dB for space marching and  $77.8$  for CFD. This example demonstrates that utilizing space marching between the near-field CFD and the far-field acoustic propagation allows significant CFD domain reduction without any loss of accuracy in ground level noise prediction. Moreover, the reduction in CFD domain size reduces the necessary grid points in the CFD grid resulting in faster turnaround time [2].

### 3.2 Unstructured CFD Solver Coupling

Coupling the space marching solver to other meshing paradigms, such as unstructured meshes, requires a generalization of the overset grid interpolation routines to CFD grid element types other than hexahedral cells. A standalone program name *Interpolator* has been developed which handles interpolating CFD solutions onto an arbitrary set of three-dimensional coordinates. Currently, hexahedral, tetrahedral, triangular prismatic, and pyramid cells are supported. Recently, an extension to arbitrary polyhedral cells is being tested using the LAVA Unstructured CFD solver, but results from this coupling will not be reported in the current work.

As part of the Third AIAA Sonic Boom Prediction Workshop [42, 43], participants were asked to submit their CFD grids and solutions along with the required workshop data. Although few participants provided the additional files, several NASA groups as well as ANSYS Canada were gracious enough to do so. One such group from NASA Langley [40], utilizing USM3D, provided their CFD solution on the committee provided mixed-element grid containing  $20,701,451$  vertices with  $14,681,692$  tetrahedra,  $146,667$  pyramids, and  $35,346,643$  prisms. Figure 10 (a) shows an isometric view of the unstructured mesh which uses prismatic cells in both the boundary layer and Mach-cone aligned extruded mesh, along with tetrahedral cells filling in the space between with pyramid cells interfacing the prisms and tetrahedra. For the space marching grid, a total of  $72,053,928$  grid points are used with  $776$  points in the space marching direction,  $513$  points in the Mach-cone aligned radial direction, and  $181$  points in the circumferential direction. In addition, a total of  $278,559$  *fringe* points are interpolated from the USM3D solution. A comparison of the unstructured and space marching grids on the symmetry plane is plotted in Figure 10 (b) - (c).

For this example, two different convective flux discretizations are compared using the space marching method. The first is a robust 4<sup>th</sup>-order centered hybrid weighted nonlinear scheme using 3<sup>rd</sup>-order WENO for the left/right state interpolation for the midpoint fluxes, denoted HWCNS4-WENO3. The second discretization uses the same 4<sup>th</sup>-order centered hybrid weighted nonlinear scheme but uses 5<sup>th</sup>-order ZWENO interpolation for the left and right states, denoted HWCNS4-ZWENO5. A standard second-order accurate flux discretization is used in USM3D with the convective fluxes approximated with HLLC and limited with the Barth-Jespersion limiter. A comparison of the pressure field on the symmetry plane between USM3D and space marching using the HWCNS4-WENO3 and HWCNS4-ZWENO5 is shown in Figure 10 (e) - (g). No visible difference can be observed in the contour plots, except at the downstream of the aft-end of the vehicle where space marching using HWCNS4-ZWENO5 appears sharper than the other two solutions. Although we could not find the reported computational resources for the USM3D solution on this mesh, the space marching solver required  $4.3$  seconds to generate the automated grid,  $8.4$  seconds to interpolate the unstructured CFD solution to the *fringe* points, and  $138.3$  seconds for HWCNS4-WENO3 and  $146$  seconds for HWCNS4-ZWENO5 to propagate the solution  $10$  body lengths. Again, all space marching simulations

were performed using 80 OpenMP threads on a modern high-end workstation. Note that only a radial domain extent of 5 body lengths was used for the unstructured mesh, limiting the potential radial coupling locations with the far-field acoustic propagation solver. This limitation is removed through coupling with the space marching solver, and in fact the radial domain of the unstructured mesh can be further reduced as demonstrated in the previous example.

For a more quantitative comparison, the on-track pressure signature at three body lengths,  $r/L = 3$ , below the aircraft is extracted from all three solutions and plotted in Figure 11. Almost no difference is observed between the CFD solutions and two space marching solutions with the exception of the wave near  $x/L = 3.85$ . A close-up of this region is shown in the upper-right inset of Figure 11. The HWCNS4-WENO3 appears to smooth this wave compared to the USM3D solution using the current space marching grid resolution. On the other-hand, the HWCNS-ZWENO5 solution captures this wave, as well as several other sharp solution features with more even resolution (i.e. less numerical dissipation) than either the HWCNS-WENO3 space marching solution or the original USM3D solution. This demonstrates how the high-accuracy and low-dissipation of the space marching solver can be used to reduce numerical discretization error in nonlinear wave propagation from the aircraft to the radial coupling location with far-field propagation code. A more complete example of this accuracy enhancement feature is illustrated in the next section.

### 3.3 CFD Accuracy Enhancement

In this section the space marching method is utilized to improve the accuracy of a CFD solution. The ANSYS Canada group, Ozcer *et. al.* [41], provided coarse, medium, and fine mixed-element unstructured grid results for the C608 test case from the Third AIAA Sonic Boom Prediction Workshop. These grids were the committee generated meshes and include a coarse mesh consisting of 11,782,783 vertices with 10,599,974 tetrahedra, 106,080 pyramids, and 19,224,816 prisms; a medium mesh consisting of 20,701,451 vertices with 14,681,692 tetrahedra, 146,667 pyramids, and 35,346,643 prisms; and a fine mesh consisting of 34,879,443 vertices with 21,266,609 tetrahedra, 146,667 pyramids, and 61,007,871 prisms. Note the medium mesh is identical to the mesh used in the USM3D coupling example in the previous section. The flow solver, HALO3D [44], is a node-centered/edge-based Galerkin finite-element method. A progressive solution strategy was used for the submitted results. To begin, the flow-field is initialized to free-stream and a first-order Roe method is used. Then the discretization accuracy is increased to a second-order Roe scheme with MUSCL and minmod limiter. The final solution is then obtained by switching to the AUSM+up scheme with MUSCL and van Albada limiter. Again, the computational time was not reported in the workshop slides.

By having access to CFD solutions on a sequence of refined meshes, the space marching solution coupled to the coarse grid CFD solution can be compared directly to the fine grid CFD solution. A space marching grid refinement study was performed using the coarse grid HALO3D solution to begin the analysis. A sequence of three space marching grids were automatically generated including a coarse 18,932,419 grid point mesh, medium 72,053,928 grid point mesh (same mesh used in USM3D coupling), and fine 280,884,850 grid point mesh. The total time to generate the automatic grids, interpolate the coarse grid HALO3D solution onto the *fringe* points and to compute the space marching solution on a workstation was 48.6 seconds for the coarse mesh, 156.7 seconds for the medium mesh, and 610.2 seconds for the fine mesh. This includes grid and solution I/O. Figure 12 plots a comparison of on-track pressure at  $r/L = 3$  between the coarse HALO3D solution and the space marching solutions from the coarse, medium, and fine grids. It is apparent from the line-plot that many of the sharp features are smoothed over in the coarse grid CFD solution. While even the coarse space marching grid is able to preserve these features even though the *fringe* points for each of the space marching solutions is interpolated from the same coarse grid HALO3D solution. In addition, no substantial difference is observed between the medium and fine space marching grid solutions. The inset image in the upper-right corner of Figure 12 shows a close-up view of the wave-train to confirm this.

Now that the medium space marching grid has been shown to be sufficient for coupling with the coarse unstructured HALO3D solution, a comparison of this space marching solution with finer mesh solutions from HALO3D are performed. Figure 13 (a) - (d) plot the on-track pressure signature at  $r/L = 2, 3, 4,$  and  $5$  body-lengths. The medium grid space marching solution is essentially equivalent to the fine unstructured HALO3D solution across the radial extraction locations. Only a minor discrepancy is observed in the recover of the nose-shock. In fact, based on the trend between the coarse, medium, and fine unstructured grid solutions

it appears the space marching solution coupled to the coarse grid HALO3D solution is more accurate than the fine grid HALO3D solution at propagating one of the wing-shocks located at  $x/L = 2.85$  for  $r/L = 2$ ,  $x/L = 3.85$  at  $r/L = 3$ ,  $x/L = 4.85$  at  $r/L = 4$  and  $x/L = 5.85$  at  $r/L = 5$ . The other discrepancy between the space marching solution and the fine unstructured HALO3D solution is observed on the aft-end of the signature at  $r/L = 5$ . Figure 14 (a) shows the pressure field on the symmetry plane along with the  $r/L = 5$  on-track extraction line from the HALO3D CFD solution. A spurious wave reflected from the outer radial boundary is pointed out using a magenta arrow and the artificial recover region downstream of the spurious wave is circled with a magenta ellipse. These non-physical solution features are not observed in the space marching solution, plotted in Figure 14 (b), and are the cause of the differences between CFD and space marching on  $r/L = 5$ . This points to another advantage of coupling space marching to near-field CFD when the CFD boundary conditions show strong boundary reflections, which will require larger radial domains than those necessary for far-field acoustic coupling. Based on this analysis, coupling the coarse unstructured grid HALO3D solution with the medium grid space marching solution results in a mid-field solution that is at least as accurate as the fine unstructured grid HALO3D solution. The mesh size difference between the coarse and fine unstructured meshes is approximately a factor of three, while the medium grid space marching method only adds 2 minutes and 37 seconds which is completely negligible, demonstrating the CFD accuracy enhancement of space marching.

### 3.4 Local Error Analysis

In the previous examples there was full-domain CFD results to compare the CFD coupled to space marching solutions to in order to verify the accuracy of the space marching method. In practice, the advantage of coupling the CFD method to space marching is fully realized when the radial extent of the CFD domain is significantly reduced. Verification of the space marching solutions, when CFD data is not available, can be performed using a similar technique as that used on full-domain CFD solutions [24]. The local error analysis method is based on a Richardson type extrapolation. One advantage of the space marching approach over general CFD methods is that a nested family of refined grids are easily generated facilitating the easy use of Richardson type methods. A second advantage of space marching is the speed of the algorithm. This allows very fine meshes to be utilized, enabling the asymptotic regime to be realized, at least in smooth parts of the flow.

Application of the local error analysis procedure is demonstrated on the JAXA Wing Body (JWB) test case from the Second AIAA Sonic Boom Prediction Workshop. The JWB is an  $L_{ref} = 38.7$  m long wing-body configuration flying at an altitude of 15.76 km, flight speed of Mach 1.6 and an angle of attack of 2.3 degrees, resulting in a flight Reynolds number of 5.7 million per meter. The CFD mesh consists of a structured overset grid with 13 zones and 14,416,429 grid points. The radial domain extent is limited to  $R/L = 0.47$  and a new adaptive redistribution algorithm, being developed by Chase Ashby from U. of Kentucky, has been applied to the off-body grid which maintains Mach-cone alignment, see Figure 15. For the space marching analysis, a family of nested refined grids were generated including a coarse grid with 22,746,813 grid points, medium grid with 87,374,673 grid points, fine grid with 342,664,675 grid points, and a reference grid with 1,356,638,802 grid points. The space marching analysis, including automated mesh generation, CFD solution interpolation, and the single sweep space marching solution procedure, required 53.1 seconds for the coarse grid, 189.1 seconds for the medium grid, 752.3 seconds for the fine grid, and 3366 seconds for the reference grid. All computations performed using 80 OpenMP threads on a modern high-end workstation. The reference mesh solution is a good example of the speed of the algorithm, requiring less than one hour to compute a solution with 1.3 billion grid points on a workstation.

Utilizing the Richardson-like procedure based on the  $L1$  norm [24], a point-wise local truncation error estimate is computed using the coarse, medium, and fine grid space marching solutions. Figures 16 (a) - (d) plots the on-track pressure signature from the fine (red) and reference (black) grid solutions along with the local error estimate (pink) at  $r/L = 2.55$ ,  $r/L = 3$ ,  $r/L = 6$ , and  $r/L = 9$ . An inset in the upper-right corner is included in each figure showing a close-up of shocks propagated from the wing-fuselage interaction region. First, it is observed that the reference solution over-plots the fine grid solution almost everywhere, up to plotting accuracy. Second, the reference grid solution is *contained* within the point-wise local error bounds across the signature domain for all radial extraction locations. These two observations indicate that the space marching solutions used in the local error analysis are likely within the asymptotic regime, and

that the error estimates should be accurate. Third, the relative magnitude of the local error bounds is not growing with increasing radial distance. This implies that the high order space marching discretization is not introducing additional error with increased radial distance, i.e. more than the truncation error of the discretization itself. In other words, the non-linear systems at each space marching plane are being approximately solved sufficiently well that the sub-iteration error is smaller than the truncation error.

Examining the location and magnitude of the local error estimates in Figures 16 (a) - (d) indicate high confidence in the smooth regions of the signatures. Near the shocks and high gradient regions of the signatures the error estimate increases in magnitude with a maximum just upstream of the reference solution shock location. This is caused by an effective dispersion error in the space marching direction using BDF2 discretization. Implicit dispersion relation preserving discretizations may reduce the magnitude of these error estimates, but as demonstrated in the first example they do not appear to affect the accuracy of the ground level noise estimate compared to convectional CFD. Moreover, with the speed and automation of the space marching method, these error estimates are trivial to compute and can be used for ground level noise uncertainty analysis using statistical approaches. The same can not be said for conventional CFD in which generating a consistent family of refined grids is difficult and the computational cost is not feasible for grids on the order of the fine and reference space marching solutions.

## 4 Conclusion

Algorithmic improvements to a high-order space marching method for sonic boom propagation have been presented. Modification to the automated space marching grid generation procedure to ensure a valid space marching direction as the local Mach number approaches unity was described. Generalization of the cylindrical hole cutting procedure to elliptical was also described. This allowed the interface between CFD and space marching to be moved closer to the aircraft thus reducing the accuracy and mesh resolution requirements for the CFD, in addition to reducing the necessary radial domain extent of the CFD grid. Examples of these features were shown for the C608 and JWB using LAVA CFD solutions on CFD grids with very limited radial domain extents. Extension of the overset interpolation based coupling procedure from structured overset grids to mixed-element unstructured grids was demonstrated using unstructured CFD solutions computed using USM3D and HALO3D from the Third AIAA Sonic Boom Prediction Workshop. Moreover, the accuracy enhancement capabilities of space marching were shown using the coarse unstructured grid HALO3D solution as input. By coupling this coarse CFD solution to the high-order space marching method, a solution with equivalent accuracy to the fine unstructured HALO3D solution was obtained. Note the additional expense of the space marching solution procedure, including automated mesh generation, interpolation of the CFD solution to the *fringe* points, and space marching solution only required 2 minutes and 37 seconds on a workstation. Finally, a local error analysis procedure, first developed for CFD, was applied to the space marching method for the JAXA Wing Body from the Second AIAA Sonic Boom Prediction Workshop. The error analysis showed that similar levels of uncertainty in the pressure signatures used for far-field acoustic propagation are obtained compared to CFD, but at a reduced computational cost and more automated way by using nested refined grids. In addition, results from the error analysis and a reference space marching solution computed on a grid with 1.3 million grid points indicated that the asymptotic regime was achieved and the accuracy of the error estimates.

A convincing argument for replacing the two-step, CFD coupled with far-field acoustics, to the three-step, CFD coupled to space marching coupled to far-field acoustics, was presented in Housman *et. al.* [1]. Accuracy of the three-step approach compared to the two-step approach for a low boom powered aircraft design was confirmed in Duensing *et. al.* [2]. The improvements presented in this paper allow coupling of the space marching solver to nearly any CFD solver using conventional meshing paradigms, and applied to supersonic aircraft designs over a large range of free-stream cruise Mach numbers. In fact, the three-step procedure utilizing space marching is currently being used within the NASA Commercial Supersonic Technology (CST) project and in conjunction with database generation for mission planning of the upcoming X59 Low Boom Flight Demonstrator (LBFD).

## 5 Acknowledgements

This work was partially supported by the NASA’s Aeronautics Research Mission Directorate (ARMD) Commercial Supersonic Technologies (CST) project and Transformational Tools and Technologies (TTT) project. The authors would like to thank the members of the AIAA Sonic Boom Prediction Workshop organizing committee, as well as Marian Nemec and the members of the LAVA team from NASA Ames Research Center for valuable discussions. Computer time has been provided by NASA’s Advanced Supercomputing (NAS) facility at NASA Ames Research Center.

## References

- [1] J. Housman, G. Kenway, J. Jensen, and C. Kiris. Efficient Near-Field to Mid-Field Sonic Boom Propagation Using a High-Order Space Marching Method. AIAA Paper 2019–3487, 2019.
- [2] J. Duensing, J. Jensen, J. Housman, M. Piotrowski, G. Kenway, D. Maldonado, E. Sozer, and C. Kiris. Structured Overset and Unstructured Grid Simulations for the Third AIAA Sonic Boom Prediction Workshop. AIAA Paper 2019–0471, 2021.
- [3] J. Page and K. Plotkin. An Efficient Method for Incorporating Computational Fluid Dynamics into Sonic Boom Prediction. AIAA Paper 1991–3275, 1991.
- [4] K. Plotkin and J. Page. Extrapolation of Sonic Boom Signatures from CFD solutions. AIAA Paper 2002–0922, 2002.
- [5] S. Rallabhandi and D. Mavris. New Computational Procedure for Incorporating Computational Fluid Dynamics into Sonic Boom Prediction. *Journal of Aircraft*, 44(6), 2006.
- [6] Y. Saito, T. Ukai, K. Miyakoshi, K. Ohtani, and S. Obayashi. Sonic Boom Estimation using the Multipole Method for Free-Flight Experiments. AIAA Paper 2014–0368, 2014.
- [7] A.R. George. Reduction of Sonic Boom by Azimuthal Redistribution of Overpressure. *AIAA J.*, 15(5):653–658, 1977.
- [8] G.B. Whitham. On the Propagation of Weak Shock Waves. *Journal of Fluid Mechanics*, 290, 1956.
- [9] O. Kandil, Z. Yang, and P.J. Bobbitt. Prediction of Sonic Boom Signatures using Euler-Full Potential CFD with Grid Adaptation and Shock Fitting. AIAA Paper 2016–2037, 2016.
- [10] O. Kandil, I. Ozcer, X. Zheng, and P.J. Bobbitt. Comparison of Full-Potential Propagation-Code Computations with the F-5E Shaped Sonic Boom Experiment Program. AIAA Paper 2016–2037, 2016.
- [11] S. Cheung, T. Edwards, and S. Lawrence. Application of CFD to Sonic Boom Near and Mid-Field Prediction. AIAA Paper 1990–3999, 1990.
- [12] M. Siclari and C. Darden. An Euler Code Prediction of Near to Mid-Field Sonic Boom Pressure Signatures. AIAA Paper 1990–4000, 1990.
- [13] H. Shen and D. Lazzara. A Space Marching Method for Sonic Boom Near Field Predictions. AIAA Paper 2016–2037, 2016.
- [14] S. Rubin and T. Lin. A Numerical Method for Three-Dimensional Viscous Flow: Application to the Hypersonic Leading Edge. *Journal of Computational Physics*, 9(2):339–364, 1972.
- [15] Y. Vigneron, J. Rakich, and J. Tannehill. Calculation of Supersonic Viscous Flow over Delta Wings with Sharp Subsonic Leading Edges. AIAA Paper 1978–1137, 1978.
- [16] L. Schiff and J. Steger. Numerical Simulation of Steady Supersonic Viscous Flow. AIAA Paper 1979–0130, 1979.
- [17] S. Chakravarthy and K. Szema. Euler Solver for Three-Dimensional Supersonic Flows with Subsonic Pockets. AIAA Paper 1985–1703, 1985.
- [18] D. Ota, S. Chakravarthy, and J. Darling. An Equilibrium Air Navier-Stokes Code for Hypersonic Flows. AIAA Paper 1988–0419, 1988.
- [19] S. Lawrence, J. Tannehill, and D. Chausee. Upwind Algorithm for the Parabolized Navier-Stokes Equations. *AIAA Journal*, 27(9):1175–1183, 1989.
- [20] S. Shaw and N. Qin. A Matrix-Free Preconditioned Krylov-Subspace Method for the PNS Equations. AIAA Paper 1998–0111, 1998.
- [21] N. Qin, D.K. Ludlow, B. Zhong, S. Shaw, and T. Birch. Multigrid Acceleration of a Preconditioned GMRES Implicit PNS Solver. Aiaa paper 1999–0779, 1999.

- [22] T. Birch, S. Prince, G. Simpson, and D. Ludlow. IMPNS: A Space-Marching Solver for Predicting the Aerodynamic Characteristics of High-Speed Missiles. AIAA Paper 2002-4512, 2002.
- [23] D. de Feo, N. Qin, and T. Birch. A MUSCL and WENO-PNS Approach for Vortex Dominated Flowfields. AIAA Paper 2010-0503, 2010.
- [24] G. Anderson, M. Aftosmis, and M. Nemec. Cart3D Simulations for the Second AIAA Sonic Boom Prediction Workshop. *Journal of Aircraft*, 56:896-911, 2019.
- [25] C. Kiris, J. Housman, M. Barad, C. Brehm, E. Sozer, and S. Moini-Yekta. Computational Framework for Launch, Ascent, and Vehicle Aerodynamics (LAVA). *Aerospace Science and Technology*, 55:189-219, 2016.
- [26] M. Vinokur. Conservation Equations of Gasdynamics in Curvilinear Coordinate Systems. *Journal of Computational Physics*, 14:105-125, 1974.
- [27] S. Choi, J. Alonso, and E. Ven der Weide. Numerical and Mesh Resolution Requirements for Accurate Sonic Boom Prediction. *Journal of Aircraft*, 46(4), 2009.
- [28] M. Park, R. Campbell, A. Elmiligui, S. Cliff, and S. Nayani. Specialized CFD Grid Generation Methods for Near-Field Sonic Boom Prediction. AIAA Paper 2014-0368, 2014.
- [29] X. Deng, M. Mao, Y. Jiang, and H. Liu. New High-Order Hybrid Cell-Edge and Cell-Node Weighted Compact Nonlinear Schemes. AIAA Paper 2011-3857, 2011.
- [30] T. Nonomura and K. Fujii. Robust explicit formulation of weighted compact nonlinear scheme. *Computers & Fluids*, 85:8-18, 2013.
- [31] J. Housman and C. Kiris. Slat Noise Predictions using Higher-Order Finite-Difference Methods on Overset Grids. AIAA Paper 2016-2963, 2016.
- [32] J. Housman, C. Kiris, and M. Hafez. Preconditioned methods for simulations of low speed compressible flows. *Computes and Fluids*, 38(7):1411-1423, 2009.
- [33] J. Housman, C. Kiris, and M. Hafez. Time-Derivative Preconditioning Methods for Multicomponent Flows - Part I: Riemann Problems. *Journal of Applied Mechanics*, 76(2), 2009.
- [34] J. Housman, C. Kiris, and M. Hafez. Time-Derivative Preconditioning Methods for Multicomponent Flows - Part II: Two-Dimensional Applications. *Journal of Applied Mechanics*, 76(3), 2009.
- [35] C.-W. Shu. High Order Weighted Essentially Nonoscillatory Schemes for Convection Dominated Problems. *SIAM Review*, 51(1):92-126, 2009.
- [36] R. Borges, M. Carmona, B. Costa, and W.S. Don. An improved weighted essentially non-oscillatory scheme for hyperbolic conservation laws. *Journal of Computational Physics*, 227(6):3191-3211, 2008.
- [37] P. Thomas and C. Lombard. Geometric Conservation Law and Its Application to Flow Computations on Moving Grids. *AIAA Journal*, 17(10):1030-1037, 1979.
- [38] M. Vinokur and H. Yee. Extension of Efficient Low Dissipation High Order Schemes for 3-D Curvilinear Moving Grids. In *Frontiers of Computational Fluid Dynamics*, pages 129-163. World Scientific, 2002. edited by D. A. Caughey and M. M. Hafez.
- [39] X. Deng, M. Mao, G. Tu, H. Liu, and H. Zhang. Geometric conservation law and applications to high-order finite difference schemes with stationary grids. *Journal of Computational Physics*, 230:1100-1115, 2011.
- [40] A. Elmiligui, M. Pandya, M. Carter, B. Diskin, and S. Nayani. USM3D Simulations for Third Sonic Boom Workshop. AIAA Paper 2021-0470, 2021.
- [41] I. Ozcer, J. Stokes, L. Monholand, and K. Zore. 3rd Sonic Boom Prediction Workshop Near-field Propagation. [<https://lbpw-ftp.larc.nasa.gov/sbpw3/workshop/sbpw3-talks-nearfield/11-sbpw3-ansys-ozcer.pdf>], 2021.
- [42] M. Park and M. Carter. Nearfield Summary and Analysis of the Third AIAA Sonic Boom Prediction Workshop C608 Low Boom Demonstrator. AIAA Paper 2021-0345, 2021.
- [43] M. Carter and M. Park. Nearfield Summary and Analysis of the Third AIAA Sonic Boom Prediction Workshop Shock-Plum Interaction Case. AIAA Paper 2021-0469, 2021.
- [44] J. Seguin, S. Gao, W. Habashi, D. Isola, and G. Baruzzi. A Finite Element Solver for Hypersonic Flows in Thermochemical Non-Equilibrium, Part I. *International Journal of Numerical Methods for Heat and Fluid Flow*, 29(1), 2019.

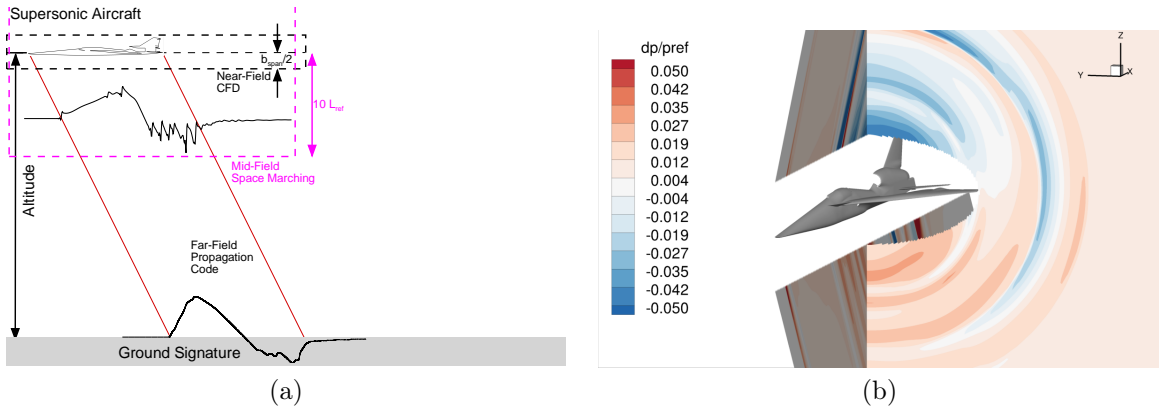


Figure 1: (a) Diagram of three-step procedure to ground level noise prediction. (b) Solution on the space marching domain showing elliptical hole cutting procedure.

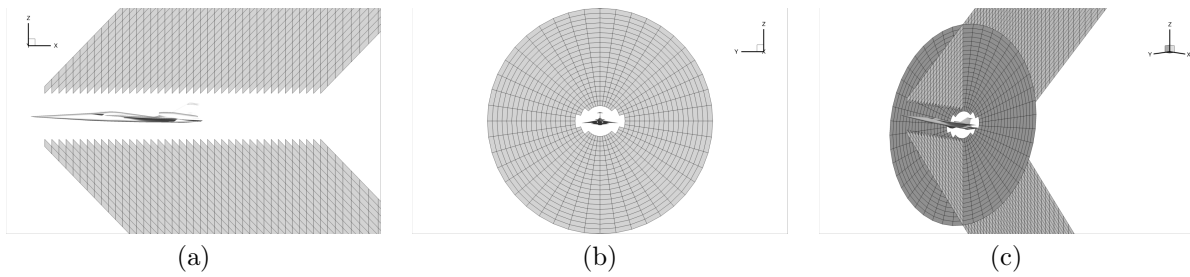


Figure 2: (a) Side view (b) front view, and (c) isometric view of a coarse space marching grid.

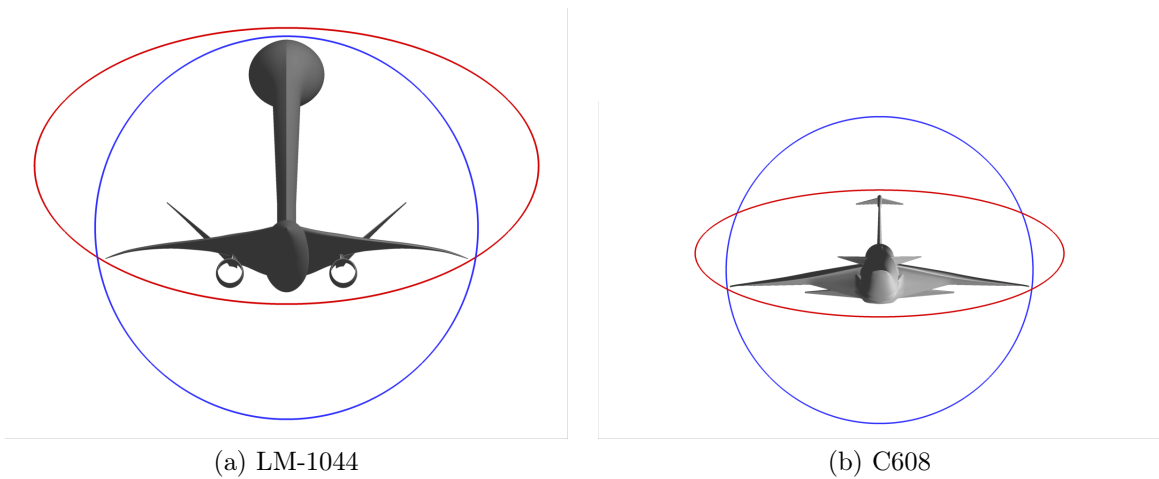
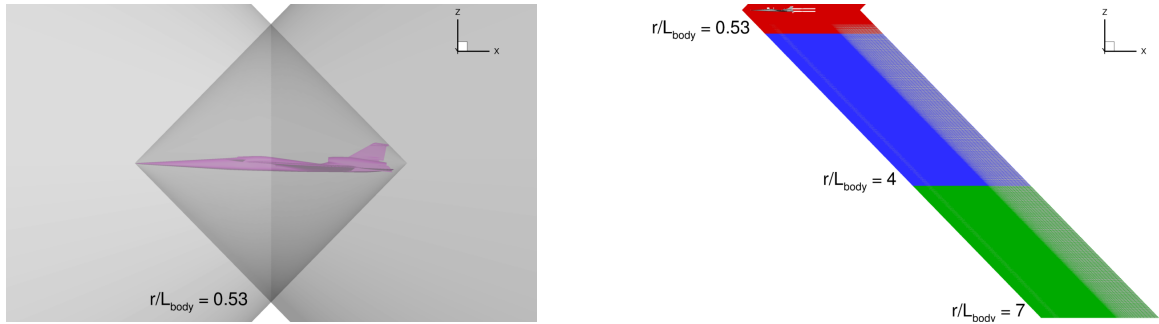


Figure 3: Comparison of cylindrical (blue) versus elliptical (red) hole cutting surfaces defining the near-field CFD and space marching interface location.



(a) Domain of dependence based on free-stream Mach cones (b) Off-body CFD grid radial extent

Figure 4: Domain of dependence and radial extent sensitivity for CFD off-body Mach cone aligned grid.

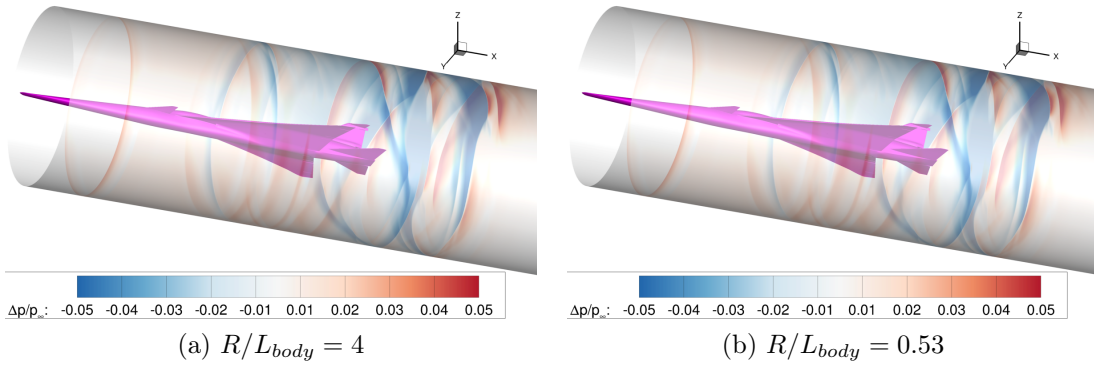


Figure 5: Plot of CFD pressure field on a cylindrical isosurface with radius  $r/L_{body} = 1/4$  using a CFD domain extent of (a) 4 body lengths and (b) 0.53 body lengths.

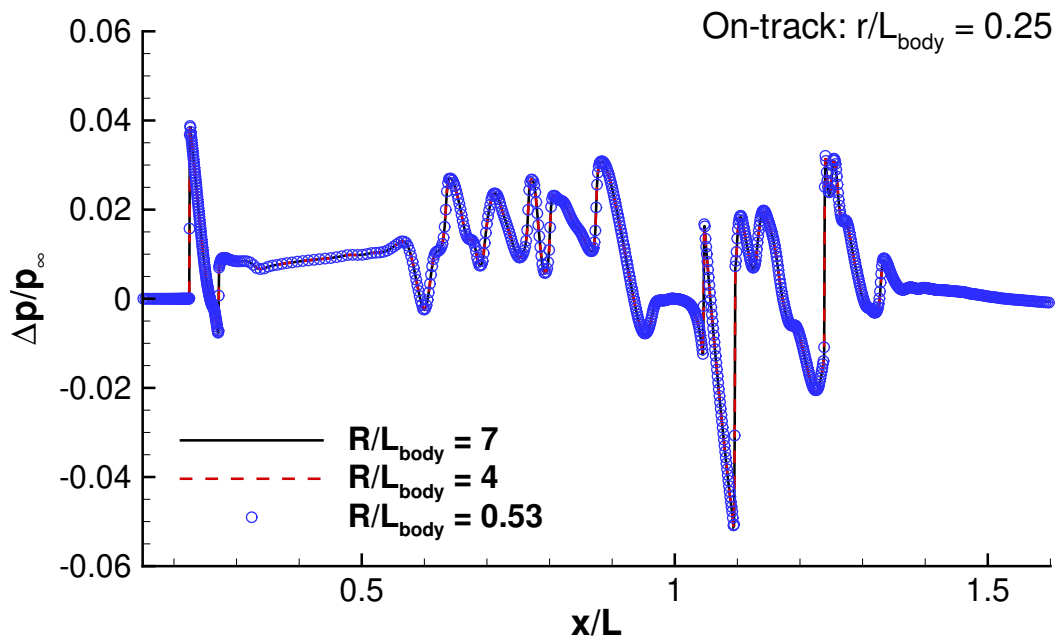


Figure 6: Plot of on-track pressure signatures using different radial domain extents at  $r/L = 1/4$ .

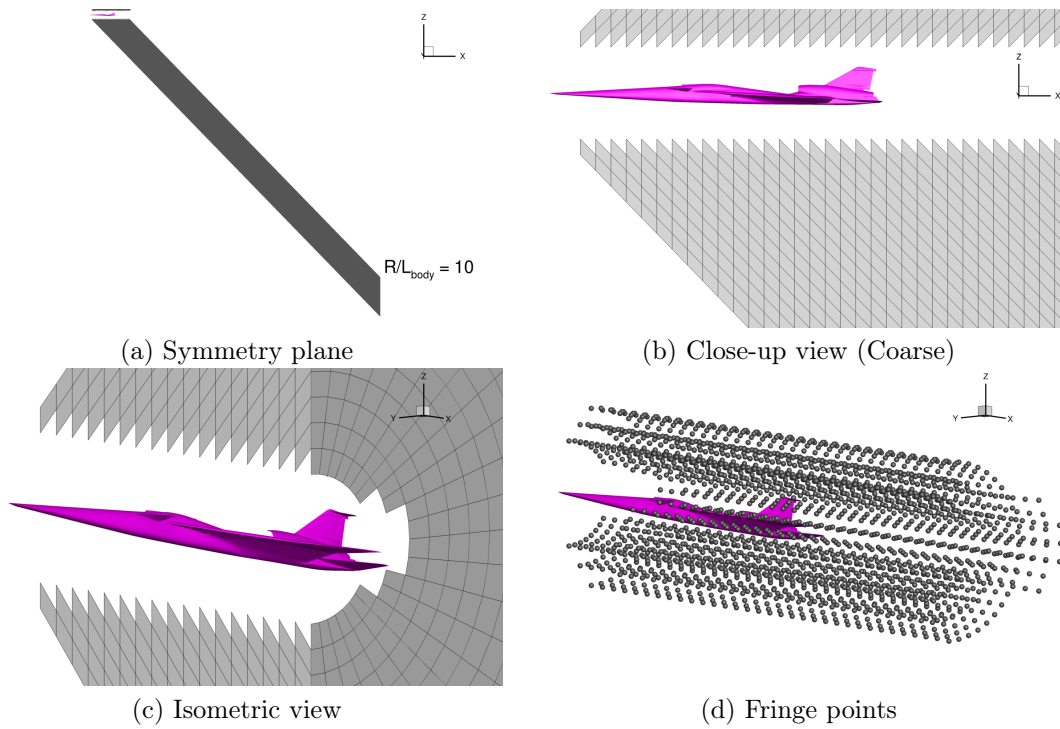


Figure 7: Images of a coarse space marching grid illustrating the elliptic hole cutting and fringe points where the CFD solution is interpolated.

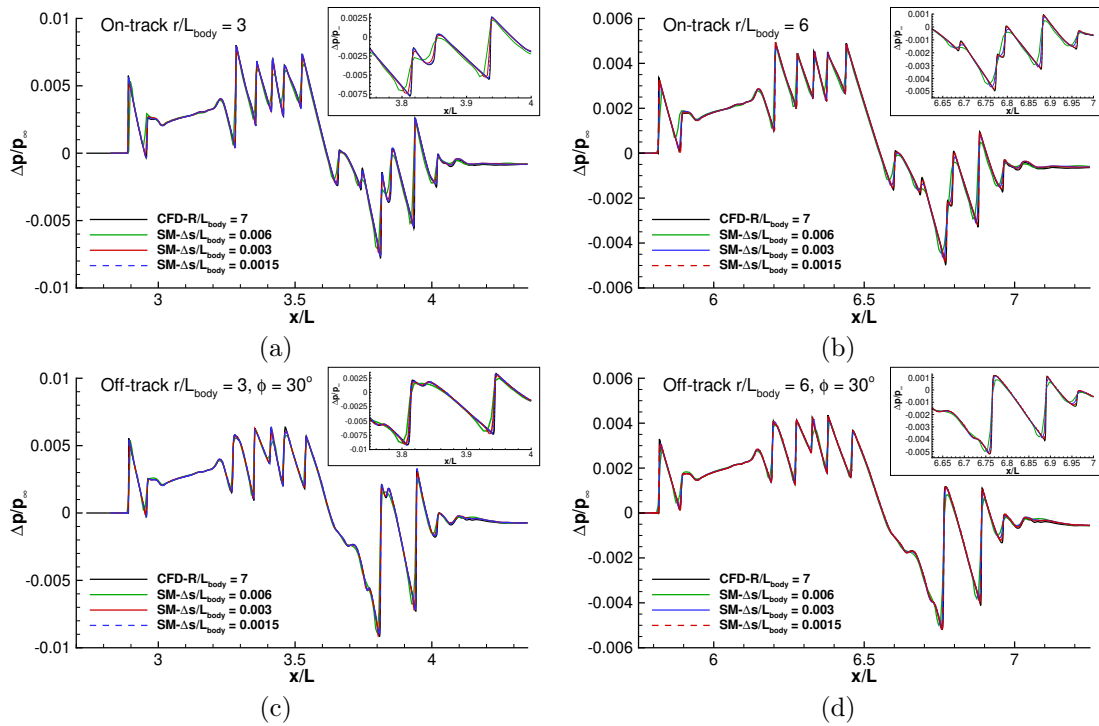


Figure 8: Comparison of pressure signatures between CFD and three space marching grid resolutions at various on-track and off-track radial locations.

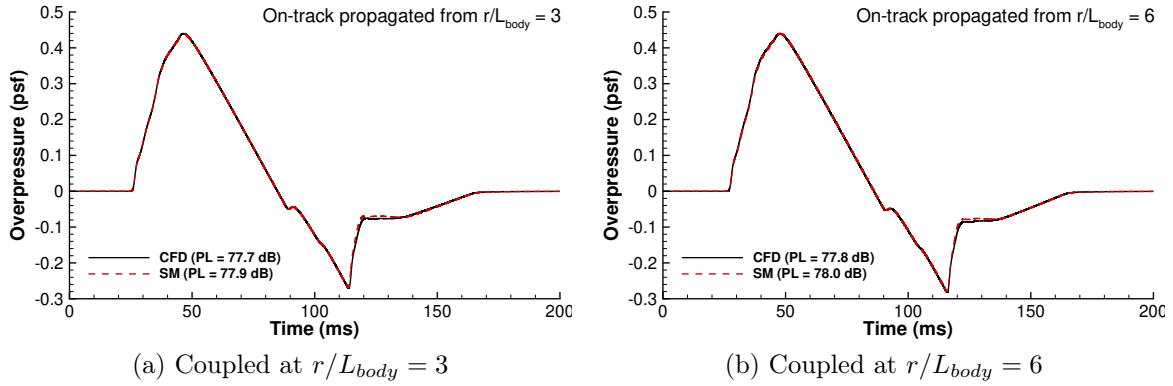


Figure 9: (a-c) Comparison of ground signatures using CFD and space marching coupled to sBoom at different radial locations. (d) Scaled near-field pressure signatures illustrating complex three-dimensional wave propagation.

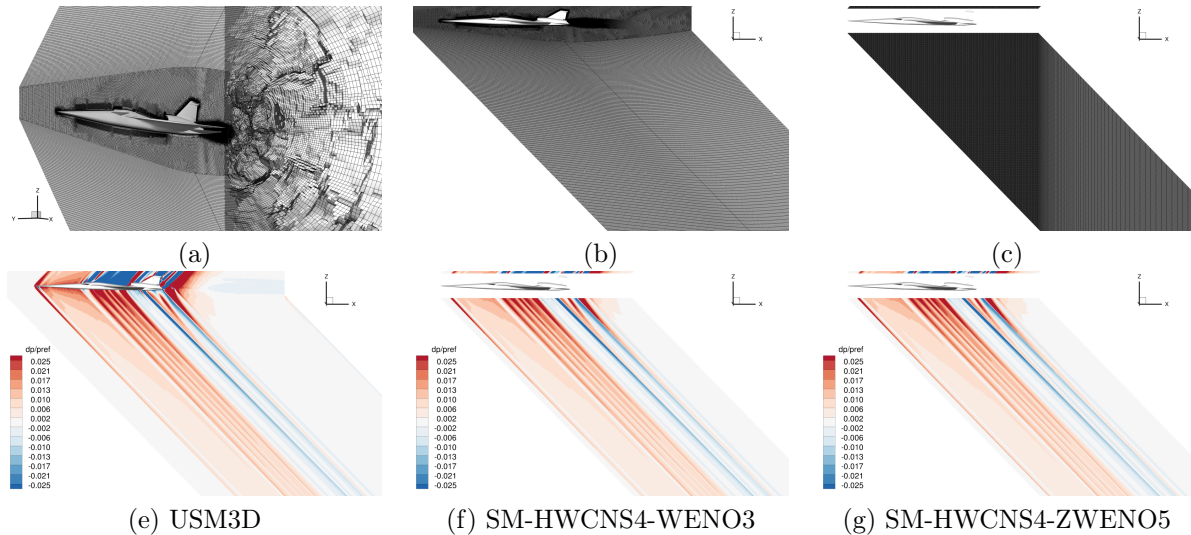


Figure 10: (a) Isometric view of the mixed-element unstructured grid. (b) Symmetry plane of the unstructured grid. (c) Symmetry plane of the space marching grid. (e-g) Pressure contours on the symmetry plane from USM3D, space marching using HWCNS4-WENO3, and space marching using HWCNS4-ZWENO5.

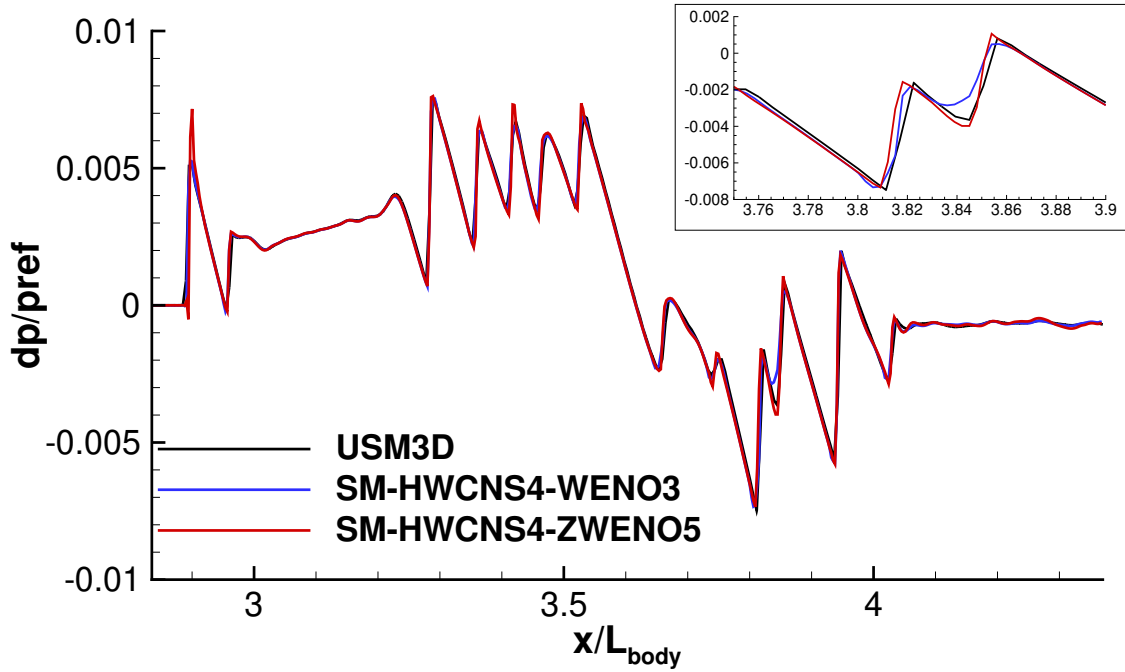


Figure 11: Comparison of USM3D on-track pressure signature at  $r/L = 3$  to space marching solutions using the baseline numerical discretization (HWCNS4-WENO3) and the low-dissipation discretization (HWCNS4-ZWENO5).

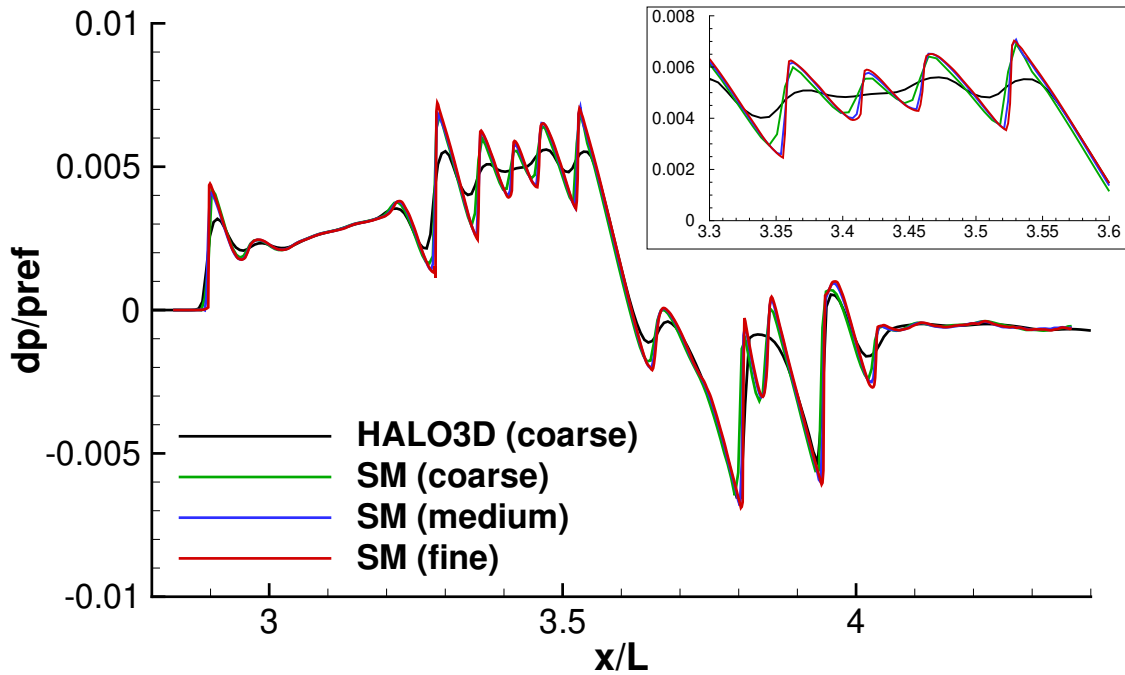


Figure 12: Comparison of HALO3D on-track pressure signature at  $r/L = 3$  using the coarse unstructured mesh to space marching solutions using coarse, medium, and fine space marching grids.

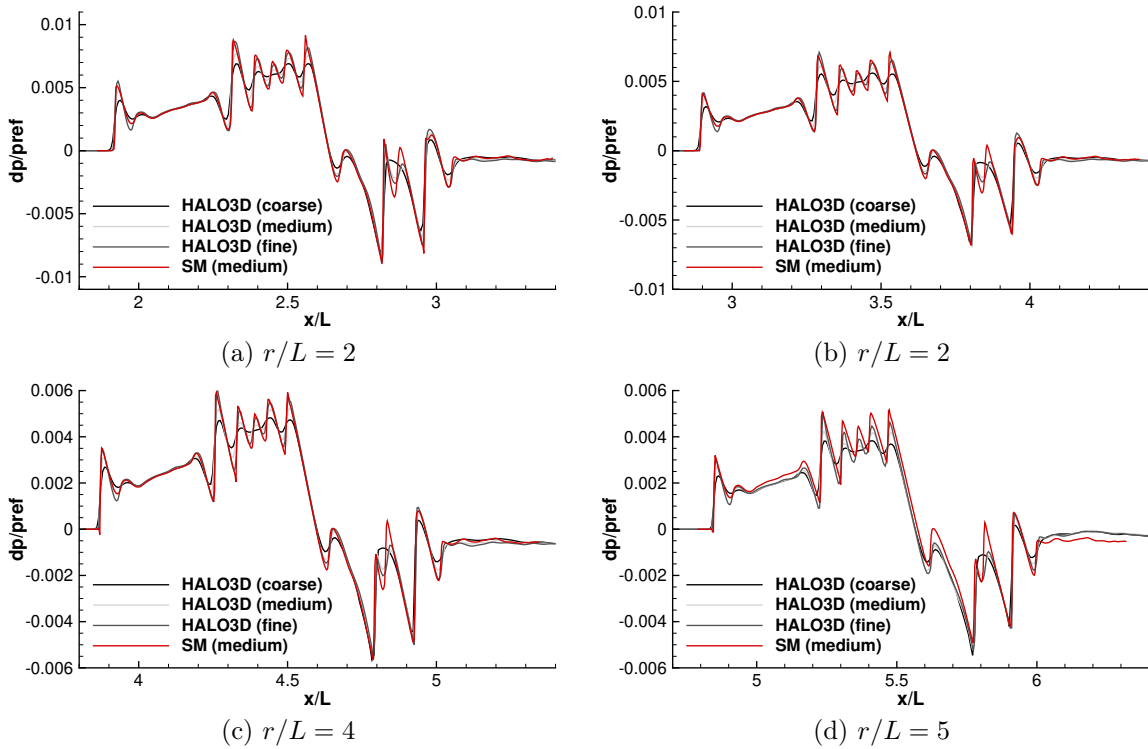


Figure 13: Comparison of coarse, medium, and fine unstructured HALO3D solutions to the medium grid space marching solution at (a)  $r/L = 2$ , (b)  $r/L = 3$ , (c)  $r/L = 4$ , and (d)  $r/L = 5$ .

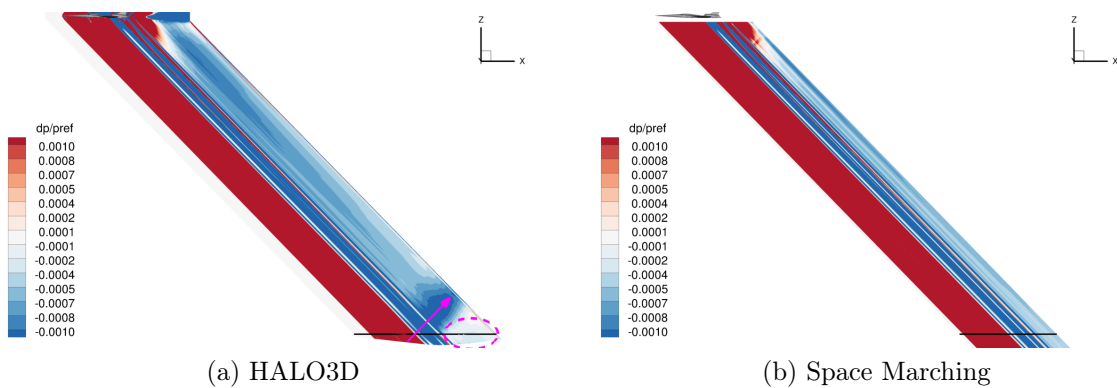


Figure 14: Pressure contour on the symmetry plane showing the  $r/L = 5$  extraction line from (a) the HALO3D solution on the fine unstructured grid and (b) the space marching solution on the medium space marching grid.

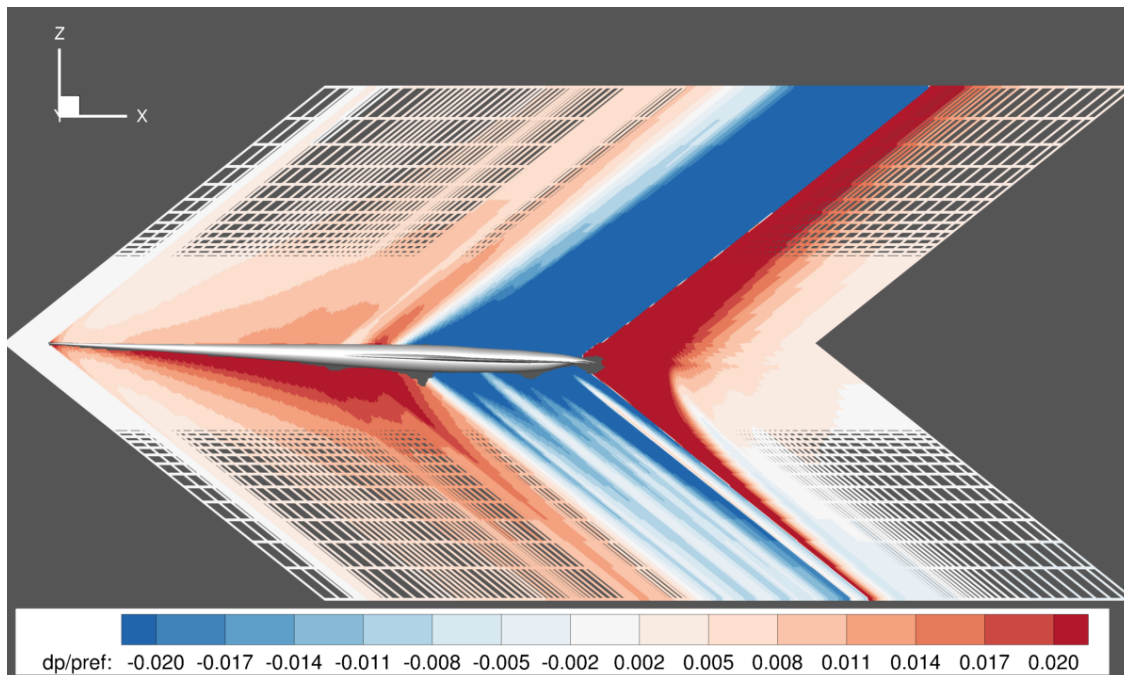


Figure 15: Plot of the off-body adapted Mach-cone aligned CFD mesh on the symmetry plane for the JAXA Wing Body (JWB) colored by pressure.

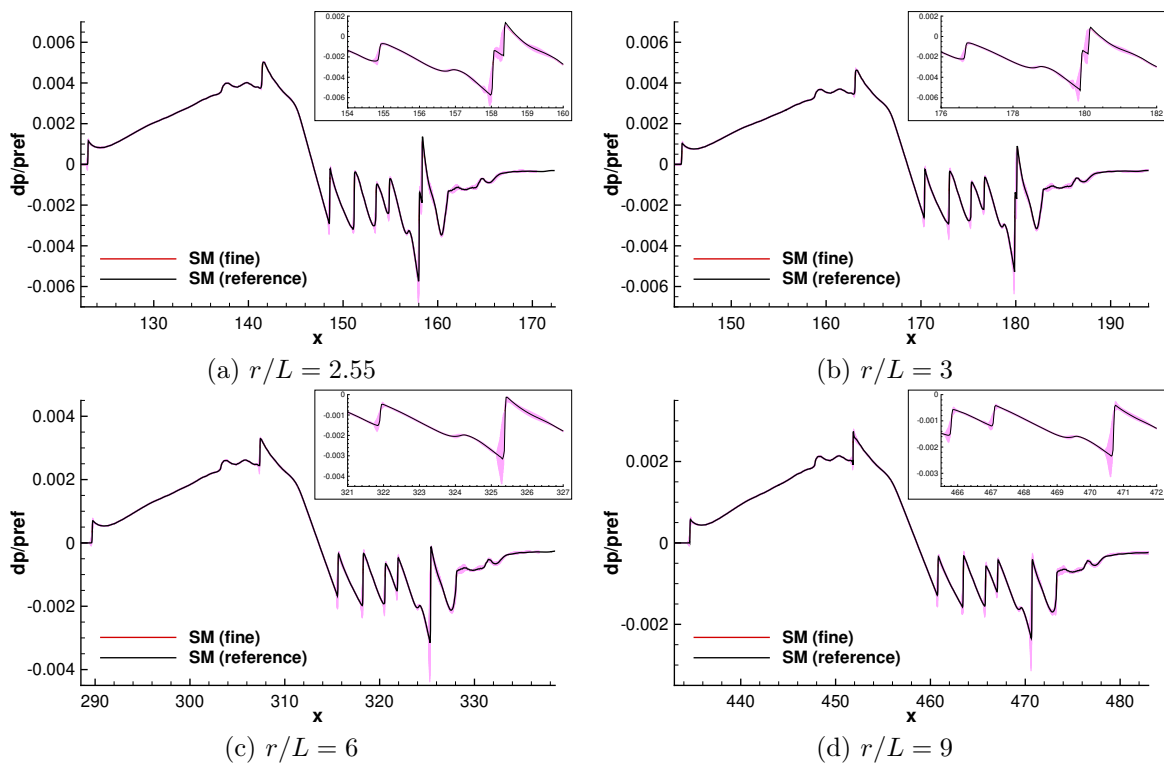


Figure 16: On-track pressure signatures plotted with local error estimate and very fine grid reference solution at  $r/L = 2.55$ ,  $r/L = 3$ ,  $r/L = 6$ , and  $r/L = 9$ .